

AE 370 Project 2

Chy-Amari Finley, Ryosuke Kawamura, Hector Ibarra and Emily Goodman
University of Illinois at Urbana-Champaign, Champaign, Illinois, 61820 Code

I. Nomenclature

A	Cross-sectional area of the beam [m ²]
E	Young's modulus [Pa]
I	Second moment of area [m ⁴]
ρ	Material density [kg/m ³]
L	Total beam length [m]
L_e	Length of a finite element [m]
Δx	Spatial discretization length [m]
x	Spatial coordinate along beam span [m]
$u(x, t)$	Transverse beam displacement [m]
$\hat{u}(x, t)$	Finite-dimensional approximation of $u(x, t)$ [m]
$\dot{u}(x, t)$	Transverse velocity [m/s]
$\ddot{u}(x, t)$	Transverse acceleration [m/s ²]
$u_k(t)$	Transverse displacement at node x_k [m]
$\theta_k(t)$	Rotation (slope) at node x_k , $\partial u / \partial x$ [rad]
$\phi_i(x)$	Global Hermite basis functions
$N_a(x)$	Local Hermite shape functions on an element
\mathcal{V}_h	Finite element approximation subspace
M	Global mass matrix [kg]
$K(t)$	Global stiffness matrix [N/m]
$M^{(k)}$	Element-level mass matrix [kg]
$K^{(k)}(t)$	Element-level stiffness matrix [N/m]
$\mathbf{u}(t)$	Global displacement vector [m]
$\mathbf{v}(t)$	Global velocity vector [m/s]
$\mathbf{y}(t)$	State vector $[\mathbf{u}, \mathbf{v}]^T$
$f(x, t)$	Distributed external load [N/m]
$\mathbf{f}(t)$	Global load vector [N]
q_0	Gust load amplitude [m/s]
ω_g	Gust excitation frequency [rad/s]
ω	Natural frequency [rad/s]
λ	Generalized eigenvalue, $\lambda = \omega^2$
$\phi_n(x)$	n th mode shape function

II. Introduction

Modern aircraft increasingly rely on lightweight, flexible wing structures to improve aerodynamic efficiency and reduce fuel consumption. A well-known example is the Boeing 787, whose composite wings are designed to flex significantly in flight, with the wingtip capable of deflecting by nearly 10% of its original span [1]. Such flexibility enhances performance but also introduces challenges in predicting structural response under dynamic loading. Accurate structural analysis is therefore essential to long-term durability. Beam theory provides a powerful framework for modeling slender aerospace structures such as wings and rotor blades. By reducing a complex three-dimensional geometry to an equivalent one-dimensional representation, engineers can rapidly estimate deflections, stresses, and vibration characteristics. This simplification is particularly valuable in the early stages of wing design, where time-dependent loads, material degradation, and aeroelastic effects must be considered without resorting to prohibitively expensive full-scale simulations.

In this project, we focus on the transient vibration response of a cantilever wing spar modeled as an Euler–Bernoulli beam with time-varying stiffness. This idealization allows us to explore how structural flexibility evolves during flight and how unsteady aerodynamic loads influence wing deflection and bending moments. By formulating the problem as an initial boundary value problem (IBVP) and applying numerical discretization techniques, we connect real-world engineering challenges to tractable academic analysis. The framework developed here sets the stage for investigating tip deflection, root bending moment, and frequency shifts, ultimately linking theoretical beam mechanics to practical aeroelastic design considerations.

III. Real-World Problem

For our real-world problem, we present an IBVP problem relevant to aerospace engineering, beam analysis. Beam theory plays a central role in the structural analysis of many slender aerospace structures and has been successfully applied to components such as rotorcraft blades, where time-dependent loads and geometric variations can be captured efficiently. Aircraft wings, though slender, introduce additional challenges due to taper, sweep, and heterogeneous internal structure, which limit the accuracy of simple analytical beam models [2, 3]. That said, beam analysis remains an essential tool in early wing design, as it reduces a complex three-dimensional structure to an equivalent one-dimensional representation that enables rapid estimation of loads, deflections, and stresses. In addition to modeling stiffness degradation or passive material variation, modern applications increasingly consider the active modulation of effective Young’s modulus through smart materials such as piezoelectric composites or adaptive laminates. These technologies enable real-time stiffness tuning for vibration suppression, load redistribution, and aeroelastic control [4]. Modern finite element beam formulations can incorporate varying cross sections, pre-twist, geometric nonlinearities, and material property variation in both space and time, as well as aeroelastic coupling. In doing so, they effectively bridge the gap between classical beam theory and far more computationally intensive three-dimensional shell or solid models [3].

Modern transport aircraft rely on long, lightweight, high aspect ratio wings whose internal load-carrying structure is dominated by spars that behave much like flexible beams in flight. As fuel is burned, both the mass distribution across the wing and the effective bending stiffness of the spar evolve, and throughout flight the structure is continually excited by unsteady aerodynamic loads arising from turbulence and maneuvers. Beyond these passive effects, emerging adaptive wing concepts seek to deliberately modify structural stiffness using actively controlled materials, allowing the effective Young’s modulus of the spar to change in response to flight conditions. Understanding how a time-dependent spar stiffness influences vibration levels, tip deflection, and internal loads is therefore critical for avoiding aeroelastic instabilities, maintaining passenger comfort, informing active load alleviation strategies, and supporting the shift toward lighter, more flexible, and morphing wing designs [5]. To study these effects within the scope of this project, we idealize the wing spar as a slender Euler-Bernoulli beam with time-varying stiffness and examine its transient vibration response under unsteady loading.

IV. Academic Problem

In the academic problem, we simplify the more complex task of predicting full aircraft wing deflection by modeling the primary load-carrying members, the wing spars, as an idealized Euler–Bernoulli beam. This approach builds directly on the real-world context described earlier and allows us to explore meaningful structural behavior using current numerical methods and structural mechanics knowledge. The resulting IBVP connects classical beam theory to physical wing responses that could be observed in flight test data, while the introduction of time-varying stiffness provides a tractable way to represent structural degradation, material softening, or adaptive structural concepts. The outputs of the

model, including tip deflection and mode frequency shifts, are quantities of direct relevance in structural and aeroelastic design. At the same time, the project provides valuable computational practice, since it requires constructing an IVP, discretizing a fourth-order partial differential equation, selecting a stable time integration scheme, and designing parameter studies that reveal how the system behaves as key inputs change.

For the model itself, we treat a cantilever wing spar as a uniform Euler–Bernoulli beam whose bending rigidity decreases linearly in time,

$$EI(t) = EI_0 \left(1 - \alpha \frac{t}{T_f}\right). \quad (1)$$

The transverse displacement $u(x, t)$ satisfies

$$EI(t) \frac{\partial^4 u}{\partial x^4} + \rho A \frac{\partial^2 u}{\partial t^2} = f(x, t), \quad (2)$$

subject to clamped root and free tip boundary conditions [6]. The beam begins from a prescribed initial shape and velocity and is excited by a simplified harmonic gust load of the form

$$f(x, t) = q_0 \sin\left(\frac{\pi x}{L}\right) \sin(\omega_g t). \quad (3)$$

Spatial discretization produces the semi-discrete system

$$M \ddot{\mathbf{u}}(t) + K(t) \mathbf{u}(t) = \mathbf{f}(t), \quad (4)$$

which is then integrated in time to examine how stiffness loss influences the vibration response. From here, a distinct physical problem of interest arises, which is to **investigate the tip response in relation to the time evolution of the structure's natural frequency**. As the stiffness matrix $K(t)$ changes over time, the associated natural frequency varies accordingly, and its evolution can be compared to the fixed forcing frequency of the gust excitation. By examining the tip displacement history alongside this frequency evolution, the response can be assessed for changes in amplitude, providing insight into resonance-like effects driven by time-varying structural properties.

A. Error properties

Even without deriving formal error bounds, the error behavior of the numerical method can be discussed using standard convergence results for Euler–Bernoulli beam discretizations and second-order time integration schemes. In this work, the beam is discretized using C^1 cubic Hermite interpolation for displacement and slope, producing a high-order spatial approximation for smooth beam responses [7]. The governing fourth-order PDE is reduced to a semi-discrete second-order ODE system, which is then integrated in time using the Newmark trapezoidal method. Based on these established properties, we expect the dominant *spatial* discretization error in the displacement response to scale approximately as

$$\|u_h - u\| \sim O(h^4),$$

provided the solution is sufficiently smooth and the time step is chosen small enough that temporal error is negligible. In practice, this implies that tip deflection and other displacement-based outputs converge rapidly under mesh refinement. However, curvature-based quantities involve additional spatial derivatives, so derived outputs such as bending moment (which depends on u_{xx}) typically converge more slowly and can be more sensitive near boundaries, even when the displacement itself shows high-order convergence. For the *temporal* discretization, the Newmark trapezoidal method is a second-order accurate scheme for linear structural dynamics, so the time integration error is expected to scale as

$$\|u_{\Delta t} - u\| \sim O(\Delta t^2),$$

assuming the response is resolved in time and the spatial mesh is sufficiently fine [8].

B. Time stepping and stability considerations

The semi-discrete system is a second-order ODE with time-dependent stiffness $K(t)$, so the choice of time step must address both accuracy and stability. In general, explicit schemes are conditionally stable and require sufficiently small Δt relative to the highest natural frequency represented on the mesh, which is often governed by the smallest element size. As a result, mesh refinement typically forces a reduction in the stable time step. Implicit schemes are widely used

in structural dynamics due to improved numerical robustness, and many commonly used implicit methods remain stable for linear problems, which is beneficial here because the stiffness $EI(t)$ decreases and the modal content of the response shifts during the simulation [8].

Even when a method is stable, Δt must still be small enough to resolve the oscillation periods of interest and to control phase and amplitude errors, particularly when studying resonance-like behavior as the evolving natural frequency approaches the gust forcing frequency ω_g . This motivates a practical time step refinement study at fixed spatial resolution, verifying that response metrics such as peak tip deflection and estimated modal frequency become insensitive as Δt is reduced. Together, the convergence and stability discussions support the interpretation that any observed resonance trends and frequency shifts arise from the modeled physics (stiffness loss and forcing) rather than numerical artifacts.

V. Numerical Methods

A. Governing PDE and boundary conditions

For the given governing PDE 2 with varying stiffness 1, gust loading conditions 3, we have clamped root and free tip boundary conditions,

$$u(0, t) = 0, \quad \frac{\partial u}{\partial x}(0, t) = 0 \quad (\text{clamped root}), \quad (5)$$

$$\frac{\partial^2 u}{\partial x^2}(L, t) = 0, \quad \frac{\partial^3 u}{\partial x^3}(L, t) = 0 \quad (\text{free tip}). \quad (6)$$

The beam starts from a prescribed initial displacement and velocity. To solve this IBVP, we employ the finite element method (FEM) for spatial discretization and the trapezoidal rule for time integration. The FEM is chosen because the governing equation involves a fourth-order spatial derivative and mixed clamped-free boundary conditions, which makes a finite difference formulation particularly cumbersome. In contrast, the FEM approach used in this course is based on an integral (energy) formulation, allowing the boundary conditions to be incorporated in a natural manner.

B. External excitation

The external excitation is modeled as a simplified harmonic gust load of the form

$$f(x, t) = q_0 \sin\left(\frac{\pi x}{L}\right) \sin(\omega_g t), \quad (7)$$

where q_0 is the load amplitude and ω_g is the gust excitation frequency.

C. Strain energy and function space requirements

As shown in Eq. (2), the bending stiffness term involves the fourth spatial derivative of the displacement. An equivalent viewpoint is obtained by considering the bending (strain) energy of the beam, which is given by

$$U(t) = \frac{1}{2} \int_0^L EI(t) (u_{xx}(x, t))^2 dx. \quad (8)$$

For the strain energy to remain finite, the second spatial derivative of the displacement must be square integrable over the domain, that is,

$$\int_0^L (u_{xx}(x, t))^2 dx < \infty. \quad (9)$$

This condition implies that the first spatial derivative u_x must be continuous throughout the domain. Consequently, the admissible approximation space for the Euler–Bernoulli beam must consist of functions whose displacement and first derivative are both continuous, i.e., the solution must belong to a C^1 -continuous function space. This observation is crucial for the choice of approximation functions in the finite element method. Standard C^0 piecewise-linear hat functions, which were introduced in the course for second-order differential equations, guarantee continuity of the displacement u but generally allow discontinuities in its first derivative. Such discontinuities give rise to singular second derivatives and therefore lead to unbounded strain energy. As a result, C^0 -continuous basis functions are not suitable for the present Euler–Bernoulli beam formulation.

D. Degrees of freedom and nodal variables

The C^1 continuity requirement directly affects the choice of nodal degrees of freedom. In order to enforce continuity of both u and u_x , the displacement field must be parameterized not only by the nodal displacement values but also by the nodal slopes [9]. Accordingly, at each node x_k we introduce two degrees of freedom:

$$u_k(t) = u(x_k, t), \quad \theta_k(t) = \frac{\partial u}{\partial x}(x_k, t), \quad (10)$$

where $\theta_k(t)$ represents the rotation of the beam cross section. As a result, the global vector of unknowns is ordered as

$$\mathbf{u}(t) = [u_0(t), \theta_0(t), u_1(t), \theta_1(t), \dots, u_N(t), \theta_N(t)]^T. \quad (11)$$

E. Finite element approximation and Hermite basis functions

The displacement field is approximated by a finite-dimensional expansion

$$\hat{u}(x, t) = \sum_{i=1}^N u_i(t) \phi_i(x), \quad (12)$$

where $\{\phi_i(x)\}$ are basis functions spanning a finite-dimensional approximation subspace of the admissible solution space.

Following the standard finite element framework introduced in the course, we define the approximation subspace \mathcal{V}_h by

$$\mathcal{V}_h = \left\{ v(x) : v \in C^1[0, L], v(0) = 0, v'(0) = 0, v|_{e_k} \in \mathbb{P}_3 \right\}, \quad (13)$$

where $e_k = [x_k, x_{k+1}]$ denotes an element (interval) of the spatial discretization and \mathbb{P}_3 is the space of cubic polynomials on each element.

This subspace incorporates the essential (clamped) boundary conditions and satisfies the C^1 continuity requirement imposed by the Euler–Bernoulli beam theory by construction.

A basis for \mathcal{V}_h is constructed using cubic Hermite beam basis functions. Each node x_k contributes two degrees of freedom: the displacement u_k and the slope $\theta_k = u_x(x_k)$. Accordingly, two global basis functions are associated with each node. Assuming a uniform mesh with spacing Δx , the global Hermite basis functions are defined in a piecewise manner, analogous to the hat functions introduced in the course [7].

For the displacement degree of freedom at node x_k , the corresponding basis function is

$$\phi_{2k-1}(x) = \begin{cases} 3 \left(\frac{x - x_{k-1}}{\Delta x} \right)^2 - 2 \left(\frac{x - x_{k-1}}{\Delta x} \right)^3, & x \in [x_{k-1}, x_k], \\ 1 - 3 \left(\frac{x - x_k}{\Delta x} \right)^2 + 2 \left(\frac{x - x_k}{\Delta x} \right)^3, & x \in [x_k, x_{k+1}], \\ 0, & \text{else.} \end{cases} \quad (14)$$

Similarly, for the slope degree of freedom at node x_k , the corresponding basis function is

$$\phi_{2k}(x) = \begin{cases} \Delta x \left[- \left(\frac{x - x_{k-1}}{\Delta x} \right)^2 + \left(\frac{x - x_{k-1}}{\Delta x} \right)^3 \right], & x \in [x_{k-1}, x_k], \\ \Delta x \left[\left(\frac{x - x_k}{\Delta x} \right) - 2 \left(\frac{x - x_k}{\Delta x} \right)^2 + \left(\frac{x - x_k}{\Delta x} \right)^3 \right], & x \in [x_k, x_{k+1}], \\ 0, & \text{else.} \end{cases} \quad (15)$$

F. Inner products and orthogonality condition

We introduce several inner products on the admissible function space V . First, we define the *energy inner product* associated with the bending strain energy as

$$(f, g)_E := \int_0^L EI(t) f''(x) g''(x) dx. \quad (16)$$

We also define the standard L^2 inner product and the *mass inner product* by

$$(f, g)_s := \int_0^L f(x) g(x) dx, \quad (f, g)_M := \rho A \int_0^L f(x) g(x) dx, \quad (17)$$

The best-approximation condition

$$\hat{u} = \min_{\tilde{u} \in \mathcal{V}_h} \|u - \tilde{u}\|_E$$

satisfies the orthogonality condition

$$(u(\cdot, t) - \hat{u}(\cdot, t), q)_E = 0 \quad \forall q \in \mathcal{V}_h. \quad (18)$$

Applying this condition with the basis functions $\{\phi_j\}_{j=1}^N$ of \mathcal{V}_h yields

$$(u(\cdot, t) - \hat{u}(\cdot, t), \phi_j)_E = 0, \quad j = 1, \dots, N. \quad (19)$$

Substituting the expansion

$$\hat{u}(x, t) = \sum_{i=1}^N u_i(t) \phi_i(x)$$

into (19) gives the projected system

$$\sum_{i=1}^N u_i(t) (\phi_i, \phi_j)_E = (u, \phi_j)_E, \quad j = 1, \dots, N. \quad (20)$$

G. Galerkin projection and semi-discrete equations

Substituting the expansion

$$\hat{u}(x, t) = \sum_{i=1}^N u_i(t) \phi_i(x)$$

into (12) gives the projected system

$$\sum_{i=1}^N u_i(t) (\phi_i, \phi_j)_E = (u, \phi_j)_E, \quad j = 1, \dots, N. \quad (21)$$

By definition of the energy inner product,

$$(u, \phi_j)_E = \int_0^L EI(t) u_{xx}(x, t) \phi_j''(x) dx. \quad (22)$$

Since $EI(t)$ depends only on time, it can be treated as a constant with respect to the spatial variable x . Integrating by parts twice with respect to x gives

$$(u, \phi_j)_E = \left[EI(t) u_{xx} \phi_j' \right]_0^L - \left[EI(t) u_{xxx} \phi_j \right]_0^L + \int_0^L EI(t) u_{xxxx}(x, t) \phi_j(x) dx. \quad (23)$$

At the clamped root, the basis functions satisfy $\phi_j(0) = \phi_j'(0) = 0$. At the free tip, the natural cantilever boundary conditions imply

$$u_{xx}(L, t) = 0, \quad u_{xxx}(L, t) = 0.$$

Hence all boundary terms in (23) vanish, yielding

$$(u, \phi_j)_E = \int_0^L EI(t) u_{xxxx}(x, t) \phi_j(x) dx. \quad (24)$$

Using the governing equation

$$EI(t) u_{xxxx}(x, t) = f(x, t) - \rho A u_{tt}(x, t),$$

we obtain

$$\begin{aligned}(u, \phi_j)_E &= \int_0^L f(x, t) \phi_j(x) dx - \int_0^L \rho A u_{tt}(x, t) \phi_j(x) dx \\ &= (f, \phi_j)_S - (u_{tt}, \phi_j)_M.\end{aligned}\tag{25}$$

The weak form leads to

$$\underbrace{\rho A \int_0^L \phi^2 dx}_{M} \ddot{q}(t) + \underbrace{EI(t) \int_0^L (\phi'')^2 dx}_{k(t)} q(t) = \underbrace{\int_0^L f(x, t) \phi(x) dx}_{F(t)}.$$

H. Element matrices and assembly

I. Interval-level mass, stiffness, and load definitions

$$M_{ab}^{(k)} := \int_{x_k}^{x_{k+1}} \rho A N_a(x) N_b(x) dx,\tag{26}$$

$$K_{ab}^{(k)}(t) := \int_{x_k}^{x_{k+1}} EI(t) \frac{d^2 N_a}{dx^2}(x) \frac{d^2 N_b}{dx^2}(x) dx,\tag{27}$$

$$f_a^{(k)}(t) := \int_{x_k}^{x_{k+1}} f(x, t) N_a(x) dx.\tag{28}$$

For the Euler–Bernoulli beam, the curvature is

$$u''(x, t) = \mathbf{B}(x) \mathbf{q}_e,$$

where

$$\mathbf{B}(x) = \frac{d^2 \mathbf{N}}{dx^2}.$$

Using $\frac{d^2}{dx^2} = \frac{1}{L_e^2} \frac{d^2}{d\xi^2}$, the second derivatives of the shape functions are

$$\begin{aligned}N_1'' &= \frac{-6 + 12\xi}{L_e^2}, \\ N_2'' &= \frac{-4 + 6\xi}{L_e}, \\ N_3'' &= \frac{6 - 12\xi}{L_e^2}, \\ N_4'' &= \frac{-2 + 6\xi}{L_e}.\end{aligned}$$

Thus,

$$\mathbf{B} = \begin{bmatrix} N_1'' & N_2'' & N_3'' & N_4'' \end{bmatrix}.$$

I. Element Stiffness Matrix

The element stiffness matrix is obtained from the bending term in the weak form,

$$\mathbf{k}_e = \int_0^{L_e} EI \mathbf{B}^T \mathbf{B} dx.$$

Changing variables to ξ gives

$$\mathbf{k}_e = EI L_e \int_0^1 \mathbf{B}^T(\xi) \mathbf{B}(\xi) d\xi.$$

For a Hermite beam element of length L_e , define the local coordinate $s \in [0, 1]$:

$$\begin{aligned} H_1(s) &= 1 - 3s^2 + 2s^3, \\ H_2(s) &= s - 2s^2 + s^3, \\ H_3(s) &= 3s^2 - 2s^3, \\ H_4(s) &= -s^2 + s^3. \end{aligned}$$

The displacement within the element is approximated by:

$$u(x) \approx \mathbf{N}(s)\mathbf{d}, \quad \mathbf{N}(s) = [H_1, L_e H_2, H_3, L_e H_4],$$

where $\mathbf{d} = [u_k, \theta_k, u_{k+1}, \theta_{k+1}]^T$ contains the nodal DOFs (displacement and rotation) [10].

The second derivative of the shape functions with respect to x is:

$$\frac{d^2\mathbf{N}}{dx^2} = \frac{1}{L_e^2} [H_1'', L_e H_2'', H_3'', L_e H_4''],$$

with

$$\begin{aligned} H_1''(s) &= -6 + 12s, & H_2''(s) &= -4 + 6s, \\ H_3''(s) &= 6 - 12s, & H_4''(s) &= -2 + 6s. \end{aligned}$$

The element stiffness matrix is defined as:

$$\mathbf{K}_e = \int_0^{L_e} EI \mathbf{N}''^T \mathbf{N}'' dx.$$

Changing variable $x = L_e s$, $dx = L_e ds$:

$$\mathbf{K}_e = EI \frac{1}{L_e^3} \int_0^1 \begin{bmatrix} H_1'' \\ L_e H_2'' \\ H_3'' \\ L_e H_4'' \end{bmatrix} \begin{bmatrix} H_1'' & L_e H_2'' & H_3'' & L_e H_4'' \end{bmatrix} ds.$$

Evaluating the integrals over $s \in [0, 1]$:

$$\begin{aligned} \int_0^1 H_1''^2 ds &= 12, & \int_0^1 H_1'' H_2'' ds &= 6, & \int_0^1 H_1'' H_3'' ds &= -12, & \int_0^1 H_1'' H_4'' ds &= 6, \\ \int_0^1 H_2''^2 ds &= 4, & \int_0^1 H_2'' H_3'' ds &= -6, & \int_0^1 H_2'' H_4'' ds &= 2, \\ \int_0^1 H_3''^2 ds &= 12, & \int_0^1 H_3'' H_4'' ds &= -6, \\ \int_0^1 H_4''^2 ds &= 4. \end{aligned}$$

Evaluating the integrals yields

$$\mathbf{k}_e = \frac{EI}{L_e^3} \begin{bmatrix} 12 & 6L_e & -12 & 6L_e \\ 6L_e & 4L_e^2 & -6L_e & 2L_e^2 \\ -12 & -6L_e & 12 & -6L_e \\ 6L_e & 2L_e^2 & -6L_e & 4L_e^2 \end{bmatrix}.$$

J. Elemental Mass Matrix

The consistent element mass matrix is obtained from [11]:

$$\mathbf{m}_e = \int_0^{L_e} \rho A \mathbf{N}^T \mathbf{N} dx = \rho A L_e \int_0^1 \begin{bmatrix} H_1 \\ H_2 L_e \\ H_3 \\ H_4 L_e \end{bmatrix} \begin{bmatrix} H_1 & H_2 L_e & H_3 & H_4 L_e \end{bmatrix} ds.$$

Evaluating the integrals over $s \in [0, 1]$ gives the standard 4x4 mass coefficients:

$$\mathbf{m}_e = \rho A \frac{L_e}{420} \begin{bmatrix} 156 & 22L_e & 54 & -13L_e \\ 22L_e & 4L_e^2 & 13L_e & -3L_e^2 \\ 54 & 13L_e & 156 & -22L_e \\ -13L_e & -3L_e^2 & -22L_e & 4L_e^2 \end{bmatrix}.$$

1. Reference interval mapping and explicit matrices

$$x = x_k + \Delta x s, \quad dx = \Delta x ds$$

$$M^{(k)} = \rho A \frac{\Delta x}{420} \begin{bmatrix} 156 & 22\Delta x & 54 & -13\Delta x \\ 22\Delta x & 4(\Delta x)^2 & 13\Delta x & -3(\Delta x)^2 \\ 54 & 13\Delta x & 156 & -22\Delta x \\ -13\Delta x & -3(\Delta x)^2 & -22\Delta x & 4(\Delta x)^2 \end{bmatrix}, \quad K^{(k)} = \frac{EI(t)}{(\Delta x)^3} \begin{bmatrix} 12 & 6\Delta x & -12 & 6\Delta x \\ 6\Delta x & 4(\Delta x)^2 & -6\Delta x & 2(\Delta x)^2 \\ -12 & -6\Delta x & 12 & -6\Delta x \\ 6\Delta x & 2(\Delta x)^2 & -6\Delta x & 4(\Delta x)^2 \end{bmatrix}.$$

2. Assembly and structure of the global matrices

The 4×4 interval stiffness and mass matrices $K^{(k)}$ and $M^{(k)}$ derived in the previous subsection represent the contribution of the interval $[x_k, x_{k+1}]$ to the global system. Each interval matrix couples the four local degrees of freedom $(u_k, \theta_k, u_{k+1}, \theta_{k+1})$.

We order the global degree-of-freedom vector as

$$\mathbf{u}(t) = \begin{bmatrix} u_0 & \theta_0 & u_1 & \theta_1 & \cdots & u_N & \theta_N \end{bmatrix}^\top.$$

With this ordering, each node is associated with a pair of degrees of freedom (u_k, θ_k) , and the global stiffness and mass matrices naturally decompose into 2×2 blocks.

For a given interval $[x_k, x_{k+1}]$, the local degrees of freedom $(u_k, \theta_k, u_{k+1}, \theta_{k+1})$ correspond to the global indices

$$(2k, 2k+1, 2k+2, 2k+3).$$

The assembly procedure consists of adding the interval matrices to the corresponding submatrices of the global system, i.e.,

$$K_{2k+i, 2k+j}(t) += K_{ij}^{(k)}(t), \quad M_{2k+i, 2k+j} += M_{ij}^{(k)}, \quad i, j = 0, \dots, 3.$$

To make the resulting structure explicit, we partition each interval matrix into 2×2 sub-blocks as

$$K^{(k)} = \begin{bmatrix} K_{LL}^{(k)} & K_{LR}^{(k)} \\ K_{RL}^{(k)} & K_{RR}^{(k)} \end{bmatrix}, \quad M^{(k)} = \begin{bmatrix} M_{LL}^{(k)} & M_{LR}^{(k)} \\ M_{RL}^{(k)} & M_{RR}^{(k)} \end{bmatrix},$$

where the blocks L and R correspond to the left node k and the right node $k+1$, respectively.

After assembling contributions from all intervals, the global stiffness matrix can be written in block form as

$$K(t) = \begin{bmatrix} K_{00}(t) & K_{01}(t) & & & \\ K_{10}(t) & K_{11}(t) & K_{12}(t) & & \\ & K_{21}(t) & K_{22}(t) & \ddots & \\ & & \ddots & \ddots & K_{N-1,N}(t) \\ & & & K_{N,N-1}(t) & K_{NN}(t) \end{bmatrix},$$

where each entry $K_{ij}(t)$ is a 2×2 block.

For interior nodes $k = 1, \dots, N - 1$, the block entries are given explicitly by

$$K_{k,k}(t) = K_{RR}^{(k-1)}(t) + K_{LL}^{(k)}(t), \\ K_{k,k+1}(t) = K_{LR}^{(k)}(t), \quad K_{k+1,k}(t) = K_{RL}^{(k)}(t).$$

All other blocks are identically zero. The global mass matrix M has the same block-tridiagonal structure, with the same assembly relations applied to $M^{(k)}$ [7].

3. Assembly of global matrices

$$\mathbf{u}(t) = [u_0, \theta_0, u_1, \theta_1, \dots, u_N, \theta_N]^T, \quad K_{2k+i, 2k+j+} = K_{ij}^{(k)}, \quad M_{2k+i, 2k+j+} = M_{ij}^{(k)}, \quad i, j = 0, \dots, 3$$

K. Trapezoidal discretization

1. Reformulation as a first-order linear system

After spatial discretization, the structural dynamics problem is governed by the second-order system

$$M\ddot{\mathbf{u}}(t) + K(t)\mathbf{u}(t) = \mathbf{f}(t).$$

To apply standard time-stepping methods, we rewrite this equation as a first-order system. Introducing the velocity $\mathbf{v}(t) = \dot{\mathbf{u}}(t)$ and defining the state vector

$$\mathbf{y}(t) = \begin{bmatrix} \mathbf{u}(t) \\ \mathbf{v}(t) \end{bmatrix},$$

the semi-discrete system can be written in the linear form

$$\dot{\mathbf{y}}(t) = A(t)\mathbf{y}(t) + \mathbf{b}(t), \quad (29)$$

where

$$A(t) = \begin{bmatrix} 0 & I \\ -M^{-1}K(t) & 0 \end{bmatrix}, \quad \mathbf{b}(t) = \begin{bmatrix} 0 \\ M^{-1}\mathbf{f}(t) \end{bmatrix}.$$

We discretize the time interval $[0, T_{\text{final}}]$ using a uniform time step Δt and define $t_n = n\Delta t$. Applying the trapezoidal rule to the first-order system (29) yields

$$\mathbf{y}_{n+1} = \mathbf{y}_n + \frac{\Delta t}{2} \left(A_n \mathbf{y}_n + \mathbf{b}_n + A_{n+1} \mathbf{y}_{n+1} + \mathbf{b}_{n+1} \right), \quad (30)$$

where $A_n = A(t_n)$ and $\mathbf{b}_n = \mathbf{b}(t_n)$.

Rearranging terms, we obtain the implicit linear system

$$\left(I - \frac{\Delta t}{2} A_{n+1} \right) \mathbf{y}_{n+1} = \left(I + \frac{\Delta t}{2} A_n \right) \mathbf{y}_n + \frac{\Delta t}{2} (\mathbf{b}_n + \mathbf{b}_{n+1}). \quad (31)$$

Thus, at each time step, the trapezoidal rule requires the solution of a linear system for the unknown state vector \mathbf{y}_{n+1} .

To determine the order of accuracy of the trapezoidal rule, we compare one time step of the numerical scheme with the exact solution using Taylor series expansions in time.

Let $\mathbf{y}(t)$ denote the exact solution of the first-order system

$$\dot{\mathbf{y}}(t) = A(t)\mathbf{y}(t) + \mathbf{b}(t).$$

Assuming that $\mathbf{y}(t)$ is sufficiently smooth in time, we expand the exact solution about t_n using a Taylor series:

$$\mathbf{y}(t_{n+1}) = \mathbf{y}(t_n) + \Delta t \dot{\mathbf{y}}(t_n) + \frac{\Delta t^2}{2} \ddot{\mathbf{y}}(t_n) + O(\Delta t^3). \quad (32)$$

Next, we consider one step of the trapezoidal rule applied to the same equation:

$$\mathbf{y}_{n+1} = \mathbf{y}_n + \frac{\Delta t}{2} (\dot{\mathbf{y}}(t_n) + \dot{\mathbf{y}}(t_{n+1})). \quad (33)$$

To compare this expression with the exact solution, we expand $\dot{\mathbf{y}}(t_{n+1})$ about t_n using a Taylor series:

$$\dot{\mathbf{y}}(t_{n+1}) = \dot{\mathbf{y}}(t_n) + \Delta t \ddot{\mathbf{y}}(t_n) + O(\Delta t^2).$$

Substituting this expansion into (33) yields

$$\mathbf{y}_{n+1} = \mathbf{y}(t_n) + \Delta t \dot{\mathbf{y}}(t_n) + \frac{\Delta t^2}{2} \ddot{\mathbf{y}}(t_n) + O(\Delta t^3). \quad (34)$$

Comparing (34) with the Taylor expansion of the exact solution (32), we observe that the trapezoidal rule reproduces all terms up to order Δt^2 . Therefore, the trapezoidal rule is second-order accurate in time.

L. Instantaneous natural frequencies

1. Generalized eigenvalue problem

At selected times $t = t_n$, we estimate the instantaneous natural frequencies of the semi-discrete system by solving the generalized eigenvalue problem

$$K(t_n) \boldsymbol{\phi} = \lambda M \boldsymbol{\phi}, \quad (35)$$

where $\lambda = \omega^2$ and ω denotes a natural frequency.

Since the mass matrix M is constant and nonsingular after eliminating the clamped degrees of freedom, we rewrite (35) as a standard eigenvalue problem by introducing the operator

$$\mathcal{L}(t_n) := M^{-1} K(t_n). \quad (36)$$

The eigenvalue problem then reads

$$\mathcal{L}(t_n) \boldsymbol{\phi} = \lambda \boldsymbol{\phi}. \quad (37)$$

In the numerical implementation (without SciPy), the action of $\mathcal{L}(t_n)$ is computed via a linear solve,

$$\mathcal{L}(t_n) = \text{solve}(M, K(t_n)),$$

and its eigenvalues are obtained using `numpy.linalg.eigvals`. Only positive eigenvalues are retained, sorted in ascending order, and the corresponding natural frequencies are computed as

$$\omega_j(t_n) = \sqrt{\lambda_j(t_n)}. \quad (38)$$

VI. Implementation

A. Overview and objective

This study investigates the transient vibration response of an Euler–Bernoulli cantilever beam whose bending stiffness decreases in time. The primary objective is to quantify how the response amplitude changes *before* and *after* the instantaneous first natural frequency $\omega_1(t)$ crosses a prescribed forcing frequency ω_g . Particular attention is paid to the response behavior following the frequency-crossing event.

B. Problem setup and fixed parameters

All parameters except the stiffness-reduction parameter α are held fixed throughout the parameter study so that observed differences in the response can be attributed primarily to changes in the stiffness evolution. Although the motivation of this study is drawn from aircraft wing structures, the present analysis does not aim to reproduce a specific aircraft configuration. Instead, representative normalized parameter values are employed to isolate the effect of time-varying stiffness on the dynamic response.

Unless otherwise stated, the baseline configuration is defined by $L = 1$, $\rho A = 1$, and $EI_0 = 1$. A harmonic distributed load of the form

$$q(x, t) = q_0 \sin(\pi x/L) \sin(\omega_g t) \quad (39)$$

is applied, with load amplitude $q_0 = 0.05$. The forcing frequency is fixed at $\omega_g = 3.4$ for all simulations.

The time-varying stiffness is modeled as

$$EI(t) = EI_0 \left(1 - \alpha \frac{t}{T_f}\right), \quad (40)$$

where $T_f = T_{\text{final}}$ denotes the total simulation time. With this choice, the stiffness decreases linearly over the entire simulation interval. For numerical robustness, $EI(t)$ is clipped to remain nonnegative.

The forcing frequency ω_g is chosen to be comparable to the initial first natural frequency $\omega_1(0)$ of the beam, such that the gradual stiffness reduction causes $\omega_1(t)$ to cross ω_g within the simulation time window. This setup enables a direct and systematic comparison of the structural response before and after the frequency-crossing event.

C. Convergence tests

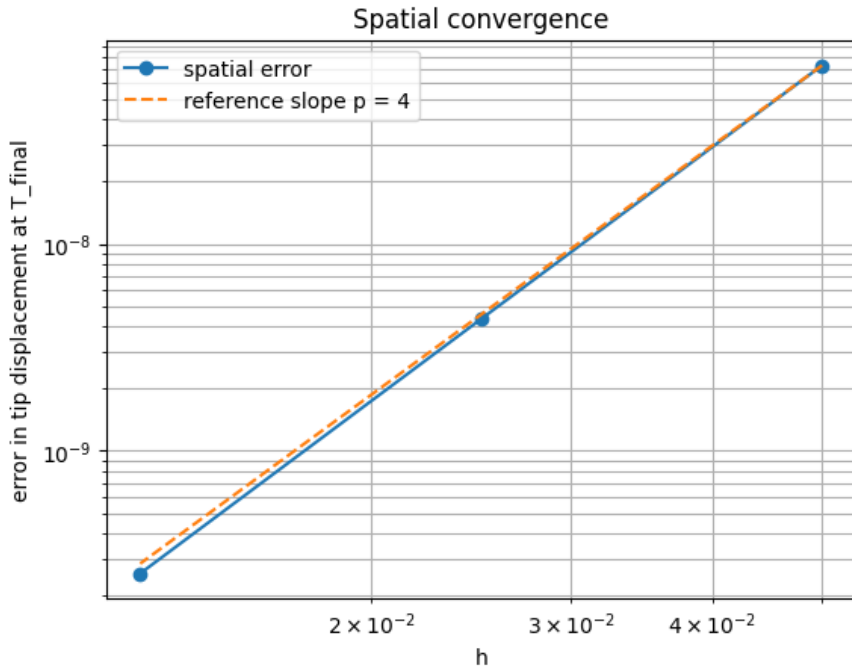


Fig. 1 Spatial convergence study for the beam tip displacement, demonstrating fourth-order accuracy consistent with Hermite beam elements.

The spatial domain $[0, L]$ is discretized using Hermite beam elements, which provide C^1 continuity suitable for the fourth-order Euler–Bernoulli beam equation. Time integration is performed using the trapezoidal rule applied to the first-order form of the semi-discrete system.

The discretization parameters used in the main simulations are chosen based on self-convergence studies. The spatial convergence study, performed over a short time window to avoid phase-accumulation effects in a dynamic response, exhibited fourth-order convergence consistent with the theoretical accuracy of Hermite elements. The temporal convergence study confirmed second-order convergence of the trapezoidal rule. Based on these results, the main analyses use

$$\text{nel} = 40, \quad \Delta t = 0.005, \quad (41)$$

which provides a suitable balance between accuracy and computational cost.

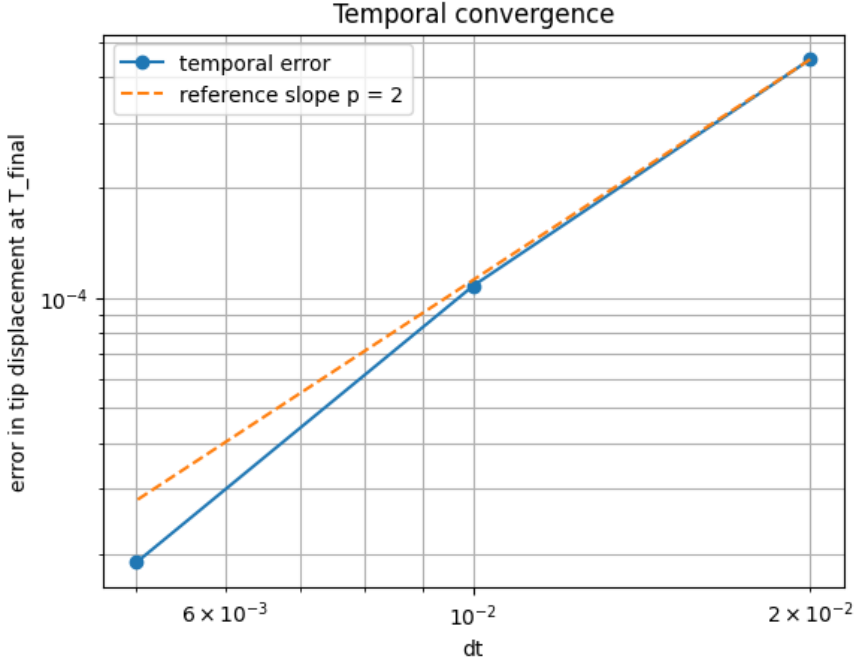


Fig. 2 Temporal convergence study for the beam tip displacement, confirming second-order accuracy of the trapezoidal time integration scheme.

D. Numerical experiment I: Constant-stiffness reference case

As a reference case, simulations with $\alpha = 0$ are first performed to establish the baseline response of a beam with constant stiffness and no frequency-crossing event. In this case, the first natural frequency remains constant in time and does not cross the forcing frequency. The resulting response serves as a control case against which the effects of time-varying stiffness can be assessed in subsequent experiments.

E. Numerical experiment II: Frequency crossing with time-varying stiffness

A representative time-varying stiffness case with $\alpha = 0.2$ is next considered to demonstrate the frequency-crossing phenomenon. For this case, the gradual reduction of stiffness causes the instantaneous first natural frequency $\omega_1(t)$ to decrease and cross the forcing frequency ω_g during the simulation. This experiment is used to verify that the numerical solver produces a stable and physically reasonable response in the presence of a frequency-crossing event, and to illustrate the characteristic response behavior associated with such a crossing.

F. Numerical experiment III: Parameter sweep and RMS-based comparison

The primary study consists of a parameter sweep over the stiffness-reduction parameter α , while all other parameters are held fixed. Varying α changes the rate at which $\omega_1(t)$ decreases and, consequently, the relative detuning between $\omega_1(t)$ and the forcing frequency ω_g . This enables a systematic investigation of how the structural response depends on the frequency-crossing event.

For each simulation, the instantaneous first natural frequency $\omega_1(t)$ is computed and the crossing time t_* is defined as the time at which

$$\omega_1(t_*) = \omega_g. \quad (42)$$

To quantitatively compare vibration levels before and after the frequency crossing, the beam tip displacement $u(L, t)$ is summarized using root-mean-square (RMS) measures. The RMS value of a signal $u(t)$ over a time interval $[t_a, t_b]$ is defined as

$$u_{\text{RMS}} = \sqrt{\frac{1}{t_b - t_a} \int_{t_a}^{t_b} u^2(t) dt}. \quad (43)$$

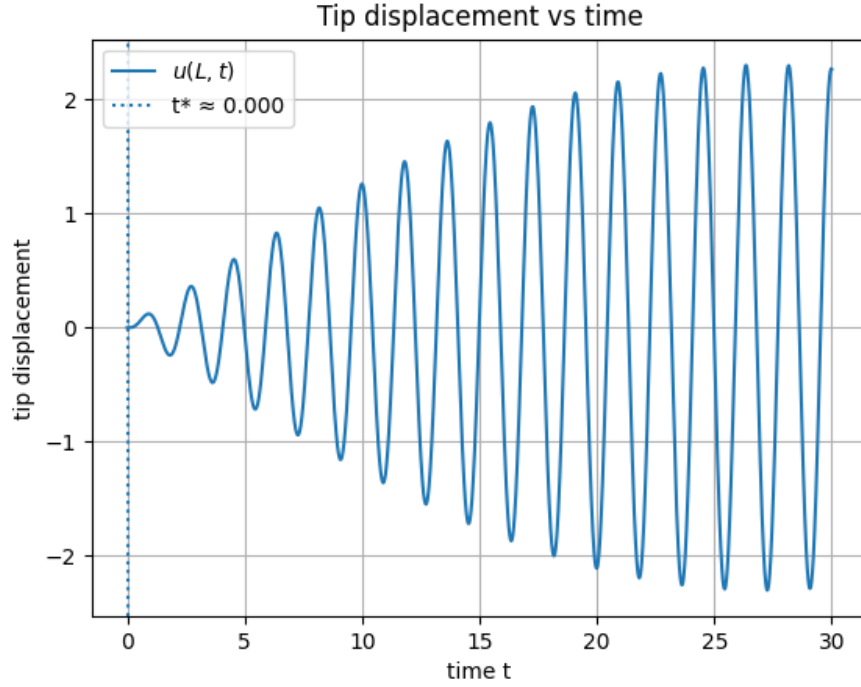


Fig. 3 Time history of beam tip displacement for the constant-stiffness case ($\alpha = 0$). The response exhibits steady forced vibration with no frequency-crossing event.

Using this definition, the pre-crossing RMS is computed over the interval $[0, t_*]$, while the post-crossing RMS is evaluated over $[t_* + \delta, T_{\text{final}}]$, where δ is a small offset introduced to exclude the immediate vicinity of the crossing time. RMS-based metrics provide a representative measure of response amplitude that is less sensitive to instantaneous phase than peak values and are therefore well suited for comparisons across different values of α .

VII. Results

A. Constant-stiffness case ($\alpha = 0$)

As a reference case, the dynamic response of the beam with constant stiffness ($\alpha = 0$) is first examined. In this case, the bending stiffness remains unchanged throughout the simulation, and the first natural frequency $\omega_1(t)$ is constant in time. Consequently, no frequency-crossing event occurs.

Figure 3 shows the time history of the beam tip displacement. The response exhibits a steady forced-vibration behavior governed by the fixed relationship between the natural frequency and the forcing frequency. This result serves as a baseline against which the effects of time-varying stiffness are assessed in subsequent cases.

B. Time-varying stiffness and frequency crossing ($\alpha = 0.2$)

Next, a representative case of time-varying stiffness with $\alpha = 0.2$ is considered to illustrate the phenomenon of frequency-crossing. As stiffness decreases over time, the first instantaneous natural frequency $\omega_1(t)$ decreases and crosses the forcing frequency ω_g during simulation.

Figure 4 shows the time history of $\omega_1(t)$ together with ω_g , clearly indicating the crossing event.

The corresponding displacement of the beam tip is shown in Figure 5. A noticeable change in the response characteristics is observed around the crossing time, motivating a quantitative comparison of the response before and after this event.

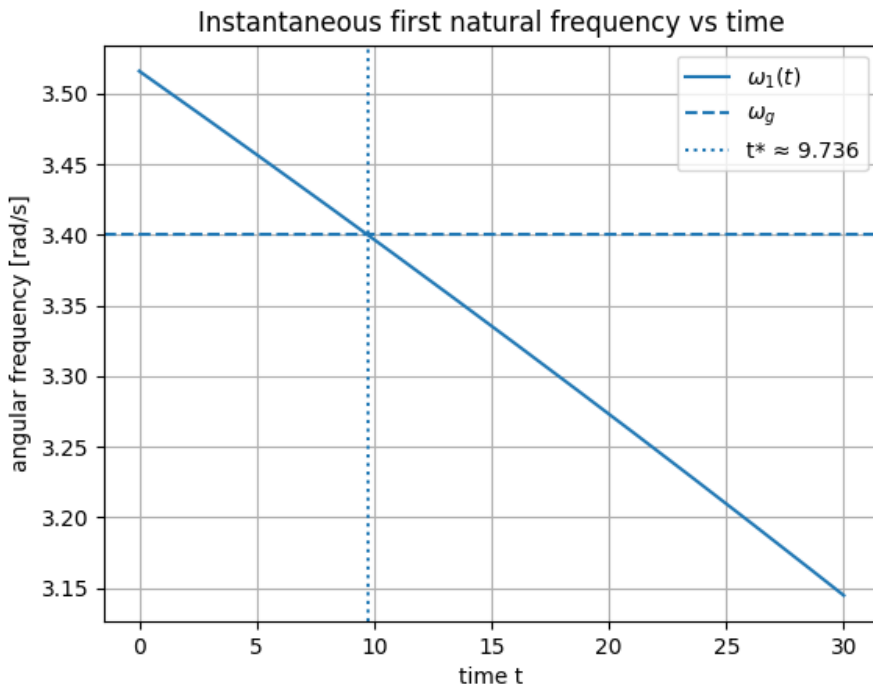


Fig. 4 Time history of the first natural frequency $\omega_1(t)$ for $\alpha = 0.2$, shown together with the forcing frequency ω_g . The crossing event is clearly observed.

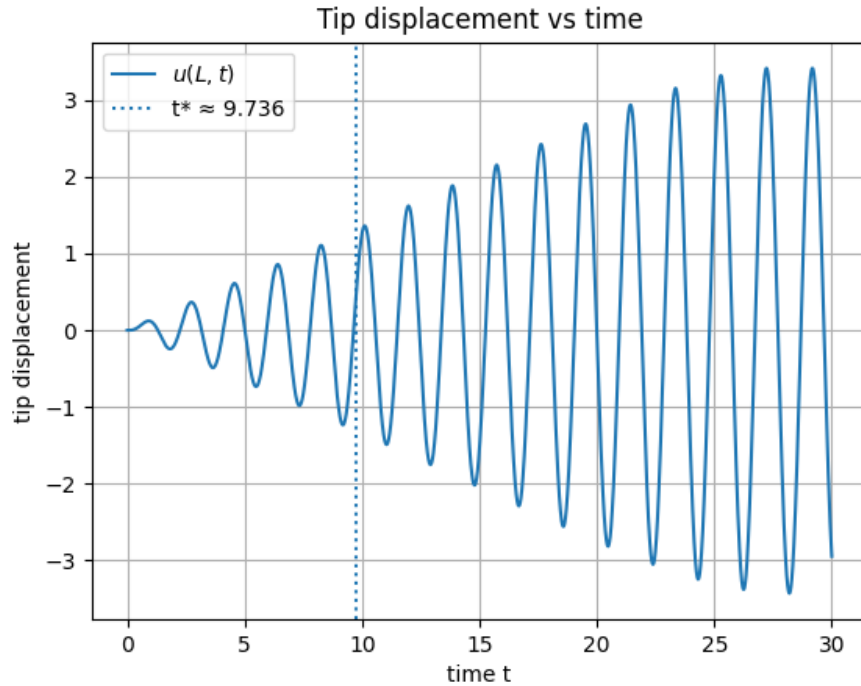


Fig. 5 Beam tip displacement response for the time-varying stiffness case with $\alpha = 0.2$. A noticeable change in response characteristics occurs near the frequency-crossing time.

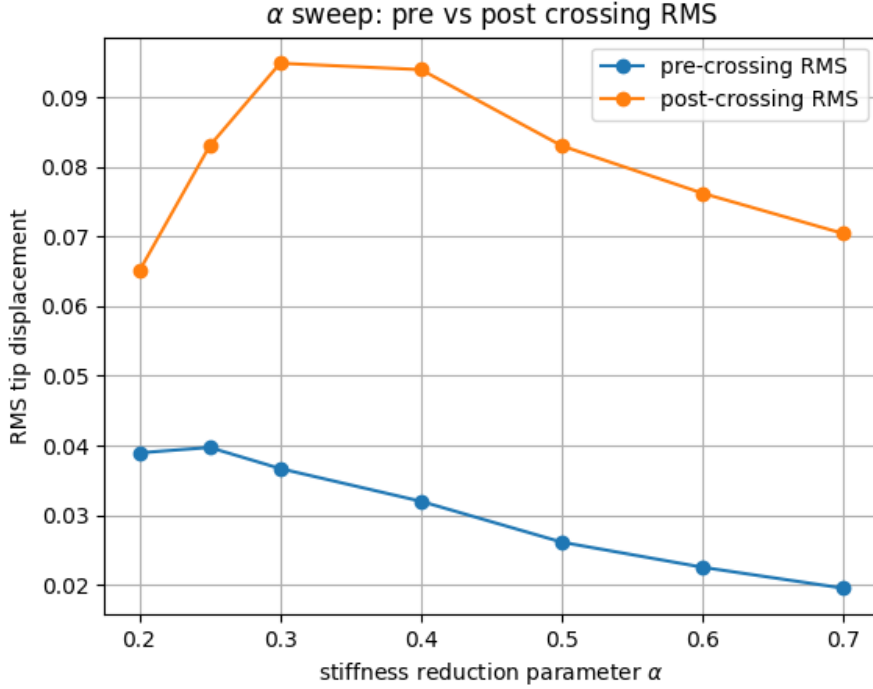


Fig. 6 Pre- and post-crossing RMS tip displacement as functions of the stiffness-reduction parameter α .

C. Effect of stiffness-reduction parameter α

To investigate the influence of stiffness reduction in a systematic manner, a parameter sweep over α is performed while all other parameters are kept fixed. For each value of α , the pre and post-crossing response levels are quantified using RMS measures of the beam tip displacement, as defined in the previous section.

Figure 6 shows the variation of the RMS values before and after crossing as functions of α . Although the pre-crossing RMS exhibits a clear dependence on α , the post-crossing RMS does not necessarily decrease even as the final natural frequency moves away from the forcing frequency.

To further characterize the final frequency separation, the absolute detuning $|\omega_1(T_{\text{final}}) - \omega_g|$ is plotted as a function of α in Figure 7. These results indicate that a large final detuning does not always correspond to a small post-crossing response amplitude.

VIII. Discussion

A. Spatial Convergence

In Figure 1, the plot shows error in the tip displacement. The blue curve represents the computed error in tip displacement at T_{final} for different mesh sizes. The points fall along a straight line on the log-log plot, sharply descending. The slope is about 4, which arose from the fact that the cubic Hermite beam elements require 4th order accuracy in displacement for smoother Euler Bernoulli beam $O(h^4)$. The smooth reduction in error indicated that the solution is well-resolved spatially for sufficiently large numbers of elements. This result certified the choice of mesh density used in the remainder of the report, and confirms that the trends observed later on were not deformed due to spatial convergence error.

B. Temporal Convergence

Figure 2 shows the effect of time step sizing on the numerical solution, with the error decreasing at about second order as Δt is reduced. This is consistent with the trapezoidal or Newmark average acceleration time integration

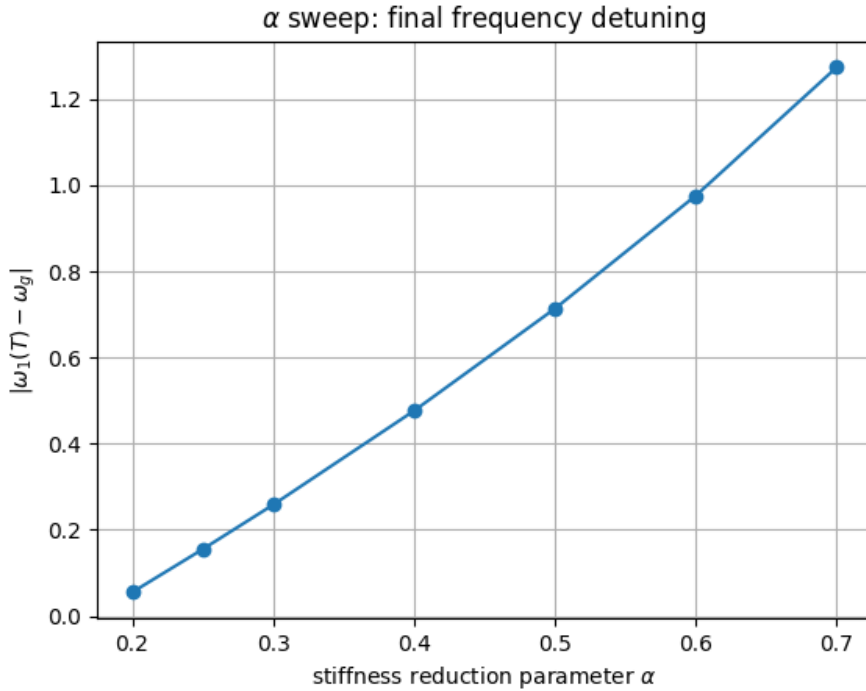


Fig. 7 Final frequency detuning $|\omega_1(T_{\text{final}}) - \omega_g|$ as a function of the stiffness reduction parameter α .

employed in the analysis, which is also second-order accurate. The clear convergence trend confirms that the chosen time step, which is $\Delta t = 0.005$, lies within the asymptotic convergence regime. Together with Figure 1, this plot establishes that both spatial and temporal discretization errors are appropriately small.

C. Constant Stiffness Baseline Response

Figure 3 shows the tip displacement time history for the baseline case, in which the bending stiffness remains constant ($\alpha = 0$). This results in a constant bending stiffness $EI(t)$. After an initial transient, the response settles into a steady oscillation at the forcing frequency ω_g . Since the stiffness and natural frequencies remain constant in this case, the system behaves as a linear time-invariant structure under harmonic excitation. Additionally, since no damping is included in the formula, the steady state oscillations persist without decay. Thus, this response provides a reference against which the time-varying stiffness cases are compared.

D. Time-Varying First Natural Frequency

Figure 4 shows the time history of the first natural frequency, $\omega_1(t)$, for a representative nonzero values of the stiffness variation parameter α . As prescribed by the stiffness model, the bending stiffness $EI(t)$ decreases linearly in time, leading to a monotonic decrease in $\omega_1(t)$. This behavior is expected since the natural frequency scales with the square root of stiffness. The figure clearly identified the time for which $\omega_1(t)$ crosses the constant forcing frequency ω_g , which is a key event governing the transient response behavior observed in the displacement histories.

E. Tip Displacement During Frequency Crossing

Figure 5 shows the tip displacement response corresponding to the stiffness variation shown in Figure 4. A clear change in the amplitude envelope occurs near the time at which $\omega_1(t) = \omega_g$. This change is caused by transient resonance as the system passes through a condition of near frequency matching between the structure and the applied harmonic load. During this interval, energy input from the forcing becomes more effective, resulting in temporary amplification of the response. Because no damping is present, the energy gained during the frequency crossing persists

after the system becomes de-tuned, leading to elevated oscillation levels beyond the crossing event.

F. Pre and Post Crossing RMS Tip Displacement

Figure 6 summarizes the influence of the stiffness variation parameter α by plotting the RMS tip displacement calculated over specified time windows before and after the frequency crossing. The pre-crossing RMS increases with α , indicating that the rate of stiffness reduction influences how the system approaches resonance and how much vibrational energy is accumulated prior to crossing. In contrast, the post-crossing RMS does not vary monotonically with α . This non-monotonic behavior demonstrates that the post-crossing vibration levels depend not only on the final system properties but also on the transient dynamics during the resonance crossing. Thus, the vibration does not settle right away, even if the natural frequency is moved far away from the forcing frequency.

G. Final Detuning as a Function of α

Figure 7 plots the final detuning between the first natural frequency and the forcing frequency, $|\omega_1(T_{final}) - \omega_g|$, as a function of the stiffness variation parameter α . As α increases, the total reduction in $EI(t)$ over the simulation time increases, resulting in larger final detuning values. However, comparison with Figure 6 shows that larger final detuning does not necessarily correspond to smaller post-crossing RMS displacement. This confirms that final detuning alone is insufficient to characterize the system response, and that the transient frequency-crossing process plays a dominant role in determining the vibration amplitude.

IX. Conclusion

In this project, the transient vibration response of a cantilever Euler–Bernoulli beam with time-varying bending stiffness was investigated under harmonic gust excitation. Using a finite element discretization with C^1 -continuous Hermite beam elements and trapezoidal time integration, the governing initial boundary value problem was solved with verified fourth-order spatial accuracy and second-order temporal accuracy. A constant-stiffness reference case ($\alpha = 0$) established a baseline forced response, while time-varying stiffness cases demonstrated how the instantaneous first natural frequency $\omega_1(t)$ decreases and crosses the fixed forcing frequency ω_g . The resulting frequency-crossing event produced clear changes in the beam tip displacement response, confirming that stiffness evolution alone can induce resonance-like transient amplification even in an otherwise linear system.

A parameter sweep over the stiffness-reduction parameter α showed that while larger values of α generally increase the final frequency detuning $|\omega_1(T_{final}) - \omega_g|$, this detuning does not uniquely determine the post-crossing vibration level. Instead, RMS-based comparisons revealed that the transient dynamics during the frequency-crossing process play a dominant role in setting the response amplitude. These results highlight the importance of accounting for time-dependent structural properties when assessing vibration behavior in flexible aerospace structures.

Contributions

Chy-Amari Finley:

Created the LaTeX document and overall report structure, developed both the real-world and academic problem sections, and wrote the code for the convergence tests.

Ryosuke Kawamura:

Contributed to the implementation of the simulation code and the derivation of the numerical method.

Hector Ibarra:

Conducted research for novel hermitian and beam methods and implementation to IBVP solution. Worked with programmers to formulate relevant matrices and error estimation models specific to the course.

Emily Goodman:

Created the introduction, discussion, and conclusion sections of the document by relating the problem to real products, presenting and interpreting the plots, and summarizing key findings in the conclusion.

Acknowledgments

We would like to acknowledge that elements of this report was aided by ChatGPT. In a collaborative groupchat made in ChatGPT, key components and questions implemented in the report were as follows:

- Discussion of IBVP ideas
- Discussion on potential guiding questions that support an iterative problem-scoping process
- Questions about how to derive DOF equation using FEM spectral analysis based on provided assumptions

Appendix

Github Repository:

https://github.com/K-Ryosuke5/AE370_Group_Project_2

References

- [1] Nguyen, N., and Precup, N., “Experimental Investigation of a Flexible Wing with a Variable Camber Continuous Trailing Edge Flap Design,” <https://ntrs.nasa.gov/api/citations/20190001600/downloads/20190001600.pdf>, November 2020. Accessed: 11 Dec. 2025.
- [2] Sarojini, D., “Structural Analysis and Optimization of Aircraft Wings Through Dimensional Reduction,” <https://repository.gatech.edu/entities/publication/e6931bdd-b456-4932-9b1c-c651110a304c>, 2021.
- [3] Agrawal, P., Dhatrak, P., and Choudhary, P., “Comparative study on vibration characteristics of aircraft wings using finite element method,” *Materials Today: Proceedings*, Vol. 46, 2021, pp. 176–183. <https://doi.org/10.1016/j.matpr.2020.07.229>.
- [4] Koko, H., and Ibrahim, G., “A Computational Framework to Optimize Piezoelectric Power Harvesting from a UAV Wing,” *Journal of Aviation Technology and Engineering (JATE)*, 2024. <https://doi.org/10.7771/2159-6670.1292>.
- [5] S, A. V., Paramasivam, R., and Vidhya, K., “Study of Optimal Design of Spar Beam for the Wing of an Aircraft,” *International Journal of Engineering Development and Research*, Vol. 5, 2017. <https://doi.org/https://doi.org/10.1016/j.istruc.2020.08.074>.
- [6] Scuciato, R., Carrer, J., and Mansur, W., “Dynamic analysis of Euler–Bernoulli beams by the time-dependent boundary element method formulation,” *Engineering Analysis with Boundary Elements*, Vol. 63, 2016, pp. 134–153. <https://doi.org/10.1016/j.enganabound.2015.11.003>.
- [7] Wang, T. S., “A Hermite Cubic Immersed Finite Element Space for Beam Design Problems,” <https://vttechworks.lib.vt.edu/server/api/core/bitstreams/4592cf6-b05c-4eal-aec5-8902f8abb1d/content>, 2005. Virginia Polytechnic Institute and State University.
- [8] Zhang, J., Liu, Y., and Liu, D., “Accuracy of a composite implicit time integration scheme for structural dynamics,” *International Journal for Numerical Methods in Engineering*, 2016. <https://doi.org/10.1002/nme.529>.
- [9] Han, L., Wang, J., Li, H., and Sun, G., “A time-domain spectral element method with C1 continuity for static and dynamic analysis of frame structures,” *Structures*, Vol. 28, 2020, pp. 604–613.
- [10] Institute of Structural Engineering, ETH Zurich, “The Euler–Bernoulli Beam,” https://ethz.ch/content/dam/ethz/special-interest/baug/ibk/structural-mechanics-dam/education/femI/2021/Lecture5_2020.pdf, 2020. Lecture notes for Method of Finite Elements I.
- [11] Felippa, C., “Lumped and Consistent Mass Matrices,” <https://quickfem.com/finite-element-analysis/>, n.d. Educational material on finite element mass matrices.